Stratigraphic analysis of an ice core from the Prince of Wales Icefield, Ellesmere Island, Arctic Canada, using digital image analysis: High-resolution density, past summer warmth reconstruction, and melt effect on ice core solid conductivity

Christophe Kinnard,[1,2] Roy M. Koerner,[1,3] Christian M. Zdanowicz,[1] David A. Fisher,[1] Jiancheng Zheng,[1] Martin J. Sharp,[4] Lindsey Nicholson,[4] and Bernard Lauriol[2]

[1] High-resolution (1 mm) stratigraphic information was derived from digital image analysis of an ice core from the Prince of Wales (POW) Icefield, Central Ellesmere Island, Canada. Following careful image processing, a profile of ice core transmitted light was derived from the greyscale images and used to reconstruct high-resolution density variations for the unfractured sections of the core. Images were further classified into infiltration and glacier ice using an automatic thresholding procedure, and were converted to a high-resolution melt percentage index. The mean annual melt percentage over the last 580 years was 9%, and melting occurred in 8 years out of 10. Melting obliterated most of the original depositional sequence, and seasonal density cycles were mostly unrecognizable. The ice core solid conductivity was greater and more variable in melt features than in glacier ice, owing to washout of strong acids by meltwater (elution) and chemical enrichment upon refreezing. This hindered the identification of acid volcanic layers and further compromised dating by annual layer counting. Comparison of the melt record with those from other Arctic ice caps shows that the melt-temperature relationship on POW Icefield is site-specific. We speculate that this is due to the peculiar position of the icefield, which rests on the periphery of the Baffin Bay maritime climate zone, and to the proximity of the North Open Water polynya, which controls snow accumulation variability on the icefield and affects the melt percentage index.

Citation: Kinnard, C., R. M. Koerner, C. M. Zdanowicz, D. A. Fisher, J. Zheng, M. J. Sharp, L. Nicholson, and B. Lauriol (2008), Stratigraphic analysis of an ice core from the Prince of Wales Icefield, Ellesmere Island, Arctic Canada, using digital image analysis: High-resolution density, past summer warmth reconstruction, and melt effect on ice core solid conductivity, *J. Geophys. Res.*, *113*, D24120, doi:10.1029/2008JD011083.

1. Introduction

[2] Visual stratigraphy is one of the most basic observations made on ice cores recovered from polar ice sheets. The visible layering in polar snow may have a depositional origin, resulting from variations in the precipitation supply and fluctuations in surface meteorological conditions [*Langway*, 1970]. The deposition of dust and pollen at the glacier surface may also form distinctive horizons in polar snow. Postdepositional processes such as the formation of depth hoar, snowmelt and subsequent percolation and refreezing of meltwater also greatly modify the snowpack structure [*Koerner*, 1997]. The preservation at depth of the original depositional sequence will depend on the intensity of these postdepositional processes. For example, in the dry snow zone of Greenland and Antarctica, a high-density wind-packed winter layer typically overlies a lower-density, coarse-grained depth hoar layer that formed during the previous summer or fall [*Alley et al.*, 1997]. This depth hoar/wind slab couplet forms a seasonal signal which can remain visible at depth, allowing for precise dating of paleoenvironmental records derived from ice cores [*Langway*, 1970; *Alley et al.*, 1997; *Meese et al.*, 1997; *Hawley et al.*, 2003].

[3] On glaciers where significant melting occurs during summer, the snowpack structure predominantly reflects the effect of melt, and any visible seasonal signal is likely to be partially or completely obliterated. On the other hand, the frequency and thickness of sporadic melt features observed in ice cores, such as ice layers and lenses, constitute useful proxies of past summer warmth [*Koerner*, 1977; *Herron et*

[1]Geological Survey of Canada, Natural Resources Canada, Ottawa, Ontario, Canada.
[2]Department of Geography, University of Ottawa, Ottawa, Ontario, Canada.
[3]Deceased 26 May 2008.
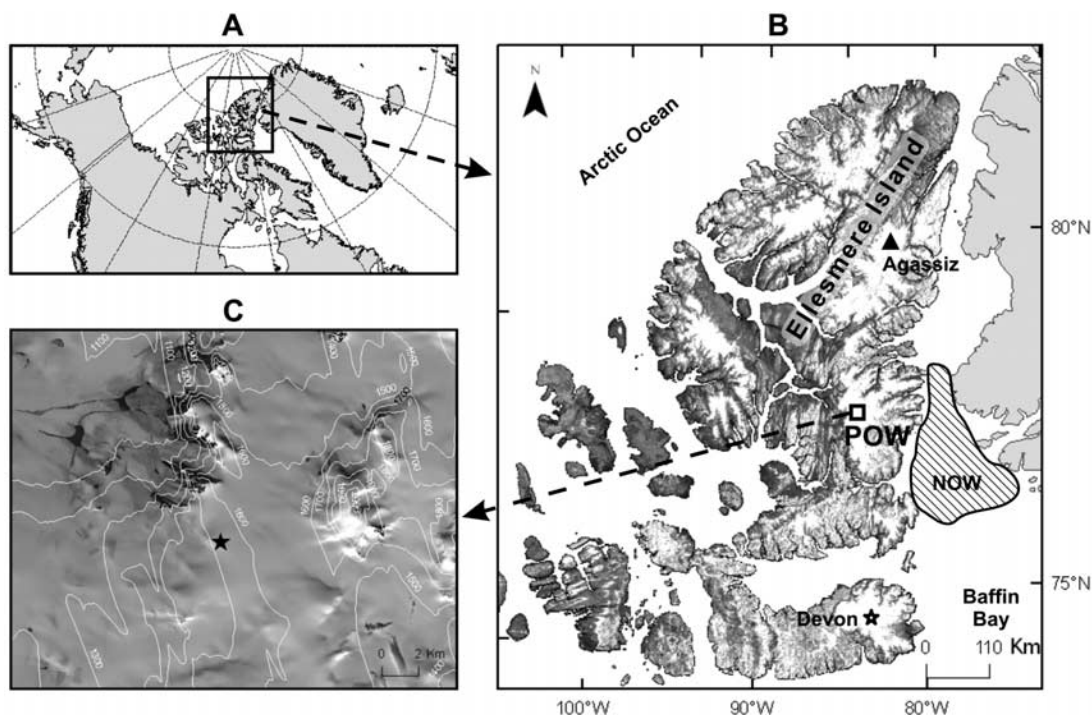[4]Department of Earth and Atmospheric Sciences, University of Alberta, Edmonton, Alberta, Canada.

Figure 1. Study area. (a) Western Arctic; (b) Ellesmere Island, with RADARSAT image overlay and ice core sites discussed in the text; and (c) drill site (star), with Landsat image overlay. Contour interval is 100 m. Satellite image and elevation data source: Natural Resource Canada.

al., 1981; *Koerner and Fisher*, 1990; *Tarussov*, 1992; *Kameda et al.*, 1995].

[4] Early studies in Greenland using ice cores photographed under transmitted light showed the potential for using the optical properties of firn and ice as a tool for stratigraphic analysis [*Langway*, 1970]. Digital image analysis of sedimentary sequences has often been used in paleolimnology and paleoceanography [e.g., *Cooper*, 1998; *Nederbragt and Thurow*, 2004] but its application to ice cores is relatively recent [*Hawley et al.*, 2003; *Takata et al.*, 2004; *Svensson et al.*, 2005; *Kaczmarska et al.*, 2006, *Sjögren et al.*, 2007]. In particular, digital image analysis can help to detect stratigraphic features that cannot be identified by the human eye. Optical data have been related to, and used to infer, physical properties of firn cores such as density [*Hori et al.*, 1999; *Hawley and Morris*, 2006; *Sjögren et al.*, 2007]. While sophisticated techniques such as three-dimensional tomography offer promising results [e.g., *Kawamura*, 1990], simpler imaging systems using charge coupled device (CCD) cameras have also proven useful [*Sjögren et al.*, 2007].

[5] The goal of this study is to derive high-resolution stratigraphic information from a new ice core from the Prince of Wales (POW) Icefield, Arctic Canada, using digital image analysis techniques. In particular, we use image analysis to derive high-resolution ice core density and a stratigraphic summer melt index [*Koerner*, 1977] in an objective and automated way. This melt index is used to investigate the effect of seasonal melting on the ice

core solid conductivity, and to characterize past summer warmth on the POW Icefield over the last 1000 years.

2. Field Sampling, Measurements, and Core Dating

[6] The POW Icefield is located in Central Ellesmere Island, Arctic Canada (Figure 1). The surface topography of the icefield is complex, with multiple domes separated by nunataks. During April–May 2005, a 176.5-m-long surface-to-bedrock ice core was retrieved from the summit of one of these domes, using an electromechanical drill. The coring site (78°23.4′N, 80°23.7′W, altitude 1630 m) has a mean annual surface temperature of −20.9°C based on the 10-m borehole temperature, while the temperature at the bottom of the borehole is −19.6°C. The accumulation rate, estimated from snow pit stratigraphy and the depth of the Katmai volcanic horizon (1912 A.D.), is approximately 0.30 m a^{-1} (ice equivalent). The coring site was chosen because of its proximity to Baffin Bay and the North Open Water (NOW) polynya, and the ice cap is expected to contain a record of past climate and sea-ice variability for the region. Detailed profiles of stable isotopes (δ^{18}O and δD) and major ion concentrations are being developed and will be presented elsewhere.

[7] Both visual and optical stratigraphic observations were conducted in the field. Each core segment recovered had a diameter of 8.3 cm and a maximum length of 100 cm. These were placed on a specially constructed light table made of a closed wooden box with two 34-W fluorescent tubes placed at the bottom (Figure 2). A half-cylindrical translucent Plexiglas receptacle was fitted within an opening
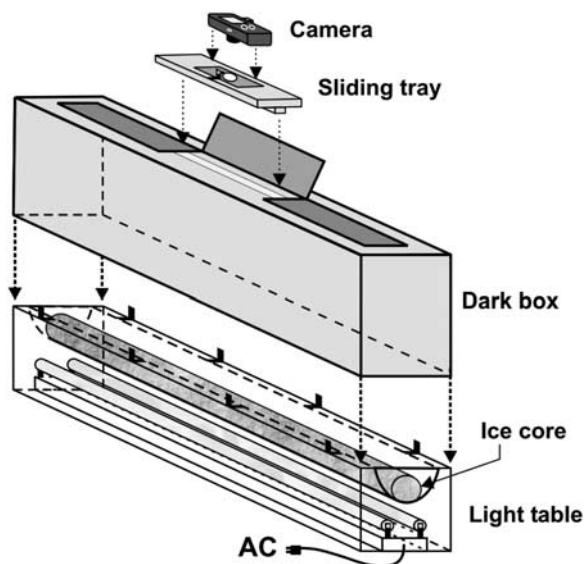
Figure 2. Light table and imaging apparatus.

in the table surface. Visual observations were made with the core segment placed in the receptacle and illuminated from below. For each core, the position and thickness of all visible melt features were recorded visually, and an estimate of the volumetric melt percentage was made for each feature with 10% accuracy. A black cardboard box was then fixed over the light table. Three overlapping images were taken of each core segment from fixed positions (hereafter called scenes 1, 2 and 3) using a Canon PowerShot S50 digital camera attached to a tray that slid along a gap atop the box. The resulting JPEG images are rectangular pixel arrays with 1944 rows and 2592 columns, with the row dimension aligned with the core axis. Each image has three 8-bit (256 tones) color channels (RGB for red, green and blue) and a resolution of 0.015 cm per pixel. Images were taken in "stitch-assist" mode, which permits visual alignment between overlapping pictures. This mode used a constant focal length of 7.1 mm and aperture value of f2.8, but the exposure time varied automatically between pictures to ensure the best image exposure.

[8] The bulk density of each core segment was measured by the gravimetric method using a top-loading scale with a precision of 0.01 kg. Solid electrical conductivity measurements of the core (ECM) [*Hammer*, 1980] were done by measuring a 1500 VDC current flowing between two brass electrodes that were moved along the core using a custom-built hand-operated device mounted on rails [*Zheng et al.*, 1998].

[9] The present core timescale is derived from a flow model [*Dansgaard and Johnsen*, 1969] "tuned" using volcanic acid layers detected by the ECM signal [e.g., *Fisher and Koerner*, 1994]. Three eruptions (Katmai, 1912 A.D., 1259 A.D. (possibly El Chichón), and Eldgjá, 934 A.D. [see *Zielinski et al.*, 1994]) were identified, as well as the Pleistocene-Holocene transition where there is a distinctive shutdown of the ECM signal, which was assigned an age of 11,700 BP using the Greenland ice core chronology [*Vinther et al.*, 2006]. The timescale was further tuned using a stacked, annually dated ECM record from

Greenland [*Vinther et al.*, 2006]. The dating error for this kind of timescale is estimated at 5% [*Kinnard et al.*, 2006].

3. Image Processing

[10] Before applying quantitative analysis, the ice core images were processed to improve image quality and correct radiometric and geometric biases. A brief outline of the processing operations is given here, and a more detailed description is provided in the auxiliary material.[1] First, RGB images were converted to single channel grey-scale images. Because the original JPEG images were not linear with respect to the voltage received by the camera CCD sensors, images had to be "linearized" using the camera response function, obtained by calibrating the camera against a Kodak gray-scale stepchart. The exposure bias resulting from varying the exposure time between images was corrected by tonally registering each linear image against a reference image. This was done by calculating the exposure ratio between each image and the reference, and then multiplying the images by their respective exposure ratio to correct the bias. Uneven background illumination in ice core images occurred owing to: (1) vignetting, a common optical defect of camera lenses; (2) interactions of the light source with the box extremities; and (3) the cylindrical shape of the cores, which resulted in increased light transmission away from the transverse core axis. The combination of these three factors produced a significant but systematic bias in the background light distribution, which needed to be removed. A data-adaptive procedure was used in which a robust polynomial surface was fitted to each image in order to estimate and remove the uneven background illumination. Finally, a radial pincushion function [*Sjögren et al.*, 2007] was used to remove the geometric ("barrel") distortion, which is another common optical defect of camera lenses.

4. Results and Discussion

4.1. Light Intensity and Ice Density Profile

[11] Following image processing, light intensity profiles were produced by averaging intensity values along a 1-cm-wide cross section at the center of each core image. Intensity profiles from scenes within the same core segment were stitched using reference marks on the light table, and all the core segment profiles were connected together afterward. The resulting depth profile of transmitted light is shown in Figure 3a. According to the Beer-Lambert Law, transmittance (T) is a reciprocal exponential function of the sample thickness (x) and the extinction coefficient (K) [e.g., *Mellor*, 1977].

$$T = \frac{I}{I_0} = e^{-x \cdot K}. \tag{1}$$

[12] Intensity variations due to varying core thickness (x) and uneven background illumination were corrected, as well as any bias due to varying exposure and incident light (I_0) (see auxiliary material). Random variations in core shape,
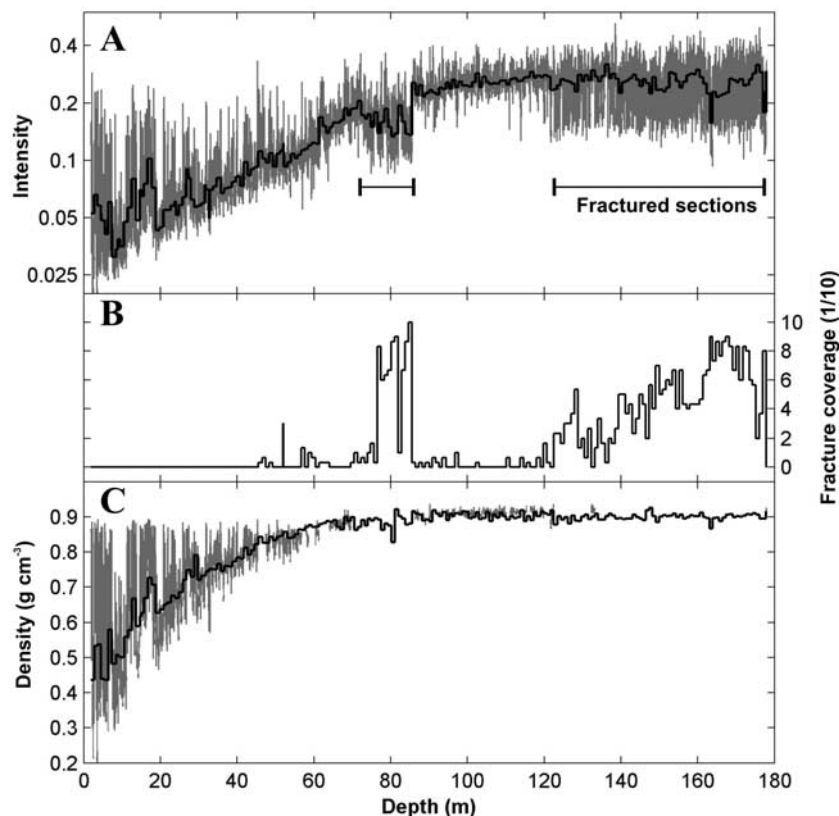
Figure 3. (a) Transmitted intensity profile (gray line) with core segment averages (black line). Profiles are shown on a logarithmic scale in accordance with equation (1); (b) core segment fracture coverage, an index of core quality; and (c) measured bulk density profile (black line) and 5-mm-interval reconstructed proxy density profile (gray line).

however, may still add noise to the transmitted light profile. The extinction coefficient K is the fraction of light lost to backscattering and absorption per unit distance within the ice core. Previous studies on the optical properties of snow reported a dependence of K on grain size and density (ρ) [*Bohren and Barkstrom*, 1974; *Mellor*, 1977; *Warren*, 1982; *Kokhanovsky and Zege*, 2004]. Optical theory for snow predicts a negative relationship between K and snow grain size; that is, light transmission increases with increasing grain size. The association with ρ is more complex, with theory predicting a positive relationship between K and ρ up to ~0.45 g cm^{-3}, after which ice becomes the dominant fraction and the relationship becomes negative [*Bohren and Barkstrom*, 1974]. The minimum bulk ρ for the POW core is close to 0.45 g cm^{-3} (black line, Figure 3c). The fact that grain size usually increases with ρ as snow ages makes it difficult to separate the influence of these two variables [*Warren*, 1982].

[13] An index of core quality (Figure 3b), ranging from 0 to 10, was calculated on the basis of the fraction of the core images covered by microfractures. These are caused by mechanical stress during ice drilling. The fractured core sections are unsuitable for stratigraphic analysis, regardless of the method used (automatic or visual).

[14] The mean light intensity profile increases steadily before leveling out at a depth of ~80 m. Because fractures increase light scattering (poor transmission), intensity values for heavily fractured core sections at 76–85 m and

beyond 120 m are not reliable. Otherwise the mean intensity profile follows closely that of the measured bulk ρ, although the rate of change in light intensity with depth is different. A scatterplot of mean light intensity against bulk ρ for cores without fractures shows that the relationship does not follow the continuous exponential function predicted by equation (1) (Figure 4). Instead, the rate of light intensity change with ice density ($\partial I / \partial \rho$) increases at specific density thresholds, which appear to correspond to different densification stages and mechanisms [*Paterson*, 1994, p.15]. During the first stage ($\rho \leq \sim0.55$ g cm^{-3}), densification is mainly due to settling, which occurs by grain-boundary sliding. The $\partial I / \partial \rho$ is small during that stage (Figure 4, stage I). In the second stage ($\rho = \sim0.55$–0.73 g cm^{-3}), densification occurs by pressure sintering, with the bounding area between grains increasing by molecular diffusion and internal deformation of crystals. The $\partial I / \partial \rho$ increases slightly during that stage (Figure 4, stage II). In the third stage ($\rho = \sim0.73$–0.83 g cm^{-3}), the contact area between grains reaches a maximum while further densification occurs by ice creep, and $\partial I / \partial \rho$ increases noticeably (Figure 4, stage III). The $\partial I / \partial \rho$ increases again sharply around 0.85 g cm^{-3} (Figure 4, stage IV), which is close to the pore close-off density (~0.83 g cm^{-3}). Beyond this threshold, air spaces are sealed, the firn has become ice and further densification occurs slowly by ice creep-induced compression of air bubbles. The relationship between I and bulk ρ was modeled by fitting a least squares piecewise linear model to the
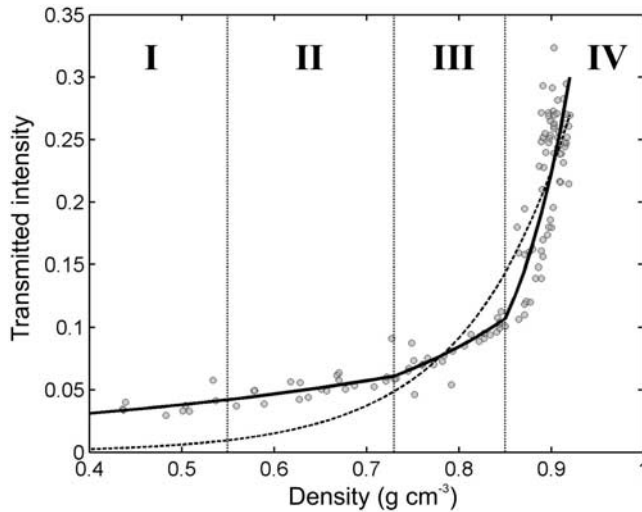
Figure 4. Mean transmitted light versus measured bulk density. The stippled line shows the theoretical relationship predicted by equation (1). The black line shows the piecewise exponential function with nodes at the main densification threshold values (dotted vertical lines with roman numbers).

log-transformed I values, with nodes at 0.55, 0.73 and 0.85 g cm^{-3}. In linear space this gives a piecewise exponential function which fits the data well ($r^2 = 0.89$), compared to the expected continuous exponential model (Figure 4).

[15] *Sjögren et al.* [2007] reported an exponential relationship between reflected light intensity and ρ similar to that observed here. *Hawley and Morris* [2006] also compared reflected intensity with density measurements from a neutron-scattering probe in a borehole at Summit, Greenland, and observed a reversal of the relationship between the two variables at ~0.55 g cm^{-3}. The nonlinear nature of the relationship between I and ρ confirms that the changing air volume is not the dominant mechanism causing the changes in the light transmission properties of the firn/ice. Because light loss occurs primarily by scattering at ice-air interfaces, the total area of these interfaces per unit volume (A/V) will determine the amount of scattering taking place. An analog measure called the specific surface area (SSA = $A/\rho_i V$, ρ_i = 0.92 g cm^{-3}) has been introduced in recent snow studies and was found to relate closely with near-infrared reflectance in surface snow [*Domine et al.*, 2008]. The SSA tends to decrease exponentially with increasing ρ but the exact relationship is unclear, and the data reported are only for $\rho <$ 0.5 g cm^{-3} [*Domine et al.*, 2008]. Three factors should decrease A/V thereby increasing light transmission: (1) rounding of individual ice particles, since a sphere has the smallest A/V ratio, (2) normal grain-growth processes (bond formation and recrystallization), and (3) rounding and compression of air bubbles within an ice matrix. In densification stage I, settling increases the number of grains per unit volume and hence A/V, and light transmission should decrease as predicted by optical theory for snow with $\rho < {\sim}0.45$ g cm^{-3}. The observed positive relationship between I and ρ during stages I and II may be explained by a decrease in A/V due to bond formation. During stage III, A/V continues to decrease, as air channels slowly become

filled by ice creep and become less tortuous [*Gow*, 1975]. Once pore close-off occurs in stage IV, air is present as irregularly shaped bubbles which become progressively smaller and more spherical under pressure [*Gow*, 1969, 1975]. Hence while the total density change during that stage is only about 0.09 g cm^{-3}, the concurrent change in microstructure and decrease in A/V strongly affects light transmission.

[16] Assuming that light transmission is related to firn density via the change in ice-air interface area, the modeled relation between mean intensity and bulk density was used to estimate high-resolution proxy density changes for the unfractured section of the POW core (Figure 3c). This approach is similar to that recently used by *Sjögren et al.* [2007]. The high-resolution (5 mm) proxy density profile shows increasing variability near the surface. This is due to the melt conditions at the site that cause refreezing of meltwater and accelerate densification in the upper layers of the icefield. Both the intensity and proxy density profiles were inspected for the presence of possible seasonal cycles, both visually and using wavelet analysis techniques. Some cycles were found in parts of the core where melt was low, but these were too sporadic to be useful for dating purposes. Therefore the original depositional stratigraphy at the POW coring site has been largely obliterated by melt, and optical stratigraphy cannot be used to date the ice core as was done elsewhere [*Hawley et al.*, 2003; *Svensson et al.*, 2005].

4.2. Facies Classification

[17] Owing to the large response of transmitted light to air bubbles, the less bubbly infiltration ice is more transparent than glacier ice, which makes it possible to distinguish melt features deep in the core. Here the term infiltration ice refers to features (layers, glands, etc.) caused by melting and refreezing. Distinguishing between infiltration ice and glacier ice (or firn) by visual interpretation is a subjective procedure that is prone to interpretation errors. Hence a method that can identify melt features automatically and objectively in an ice core is desirable. In order to distinguish ice facies using transmitted light intensity, we seek an optimal threshold that best discriminates between two populations of pixel intensity. This scheme assumes that the intensity contrast is largest between the two ice facies. This assumption corresponds to visual observations, namely that the contrast between infiltration ice and glacier ice is larger than between other facies, such as depth hoar and wind slab layers. Here we use the minimum error thresholding algorithm (MET) of *Kittler and Illingworth* [1986], the performance of which has been found to surpass that of many other algorithms in the literature [*Sezgin and Sankur*, 2004]. The MET procedure assumes that the image probability density function $p(I)$, approximated by the intensity histogram, represents a mixed, two-class population of pixels that can be divided into objects (infiltration ice) and background (glacier ice). Hence, we have

$$p(I) = \sum_{i=1}^{2} P_i p(I_i), \qquad (2)$$

where P_i is the proportion of pixels in each class ($i = 1, 2$). It is assumed that the intensity values for each of the two ice
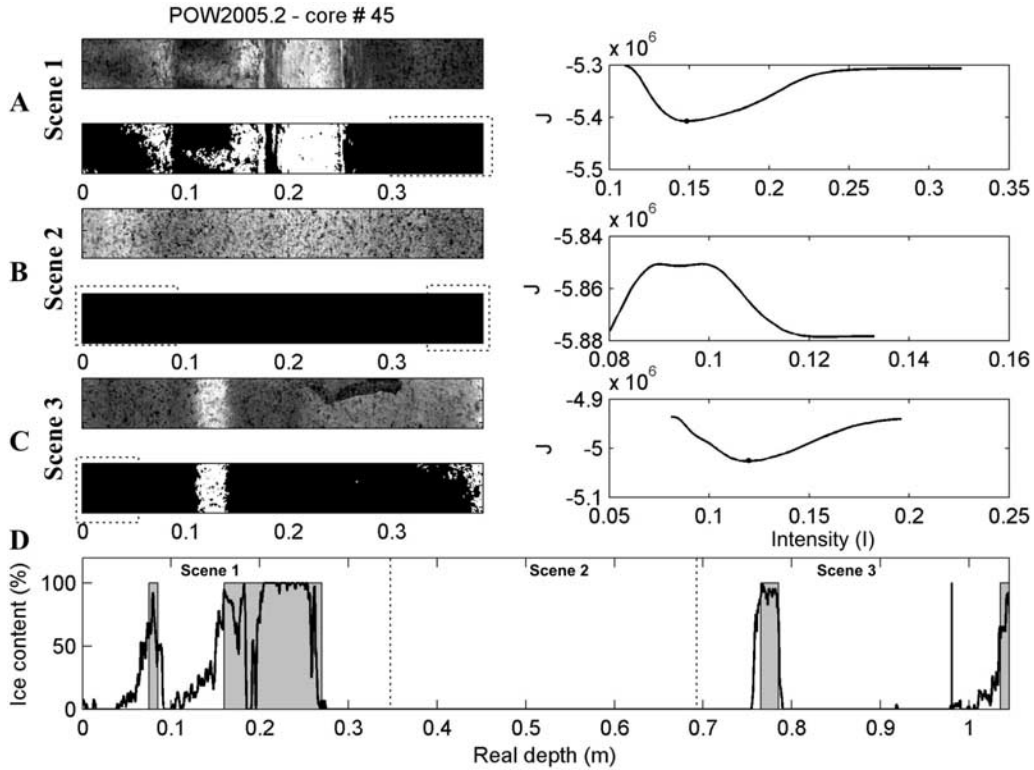
Figure 5. Results from the facies classification procedure for core 45 (45.5–46.5 m depth). (a) Original and classified core image from scene 1, with associated criterion function $J(I)$ and internal minimum corresponding to the optimal intensity threshold (black dot). (b) Same as Figure 5a, but for scene 2; $J(I)$ has no internal minimum so the whole image is classified as glacier ice. (c) Same as Figure 5a, but for scene 3. The stippled rectangles over the binary images delineate the overlapping scene areas; note the different x axis limits for $J(I)$ functions. (d) Stitched ice content index P_i (black line) and corresponding visual estimations (gray bars). Stippled vertical lines show stitching boundaries.

facies are normally distributed with mean μ_i and standard deviation σ_i. The bias in μ_i and σ_i caused by truncation of the distribution during thresholding was corrected following *Cho et al.* [1989]. The optimal separation threshold (T_{opt}) was obtained by minimizing the criterion function

$$T_{opt} = \min\left\{ J(I) = 1 \right.$$
$$\left. + \left(\frac{2[P_1(I)\log\sigma_1(I) + P_2\log\sigma_2(I)]}{-2[P_1(I)\log P_1(I) + P_2(I)\log P_2(I)]} \right) \right\}, \quad (3)$$

where the subscripts 1 and 2 correspond to the two ice facies. The cost function $J(I)$ reflects the amount of overlap between the object and background density functions. An internal minimum in $J(I)$ corresponds to the threshold that minimizes the classification error between the two components [*Kittler and Illingworth*, 1986]. For any image, if $p(I)$ is unimodal, the criterion function has no internal minimum and no threshold is returned. The whole image is then classified as glacier ice since this facies dominates. Visual verification showed that this scheme was almost always correct. Only one small (20 cm), broken core segment consisting entirely of infiltration ice had to be reclassified.

[18] The algorithm described above successfully identified melt features in the core (Figures 5 and 6). However, two situations sometimes confused the thresholding algo-

rithm and required manual editing of the binary image: (1) the presence of opened, bright cracks, mostly in the top 20 m of the core; and (2) microfractured surfaces. Cracks were mistakenly classified by the algorithm as infiltration ice and had to be edited out from the classified images. Fractures caused a third (darker) pixel population to appear in the image intensity histogram, which violated the assumption of a two-class mixed population. The core quality index, which gives the percentage of an image covered by dark microfractures, was used to remove the corresponding lower percentile from the image histogram and the MET algorithm was applied afterward. This worked well for cores with less than 60% fractures, but failed on some of the more damaged cores, which had to be thresholded manually. Noise was then removed from all classified images using morphological opening [*Russ*, 2002, p. 410], and only objects larger than 20 pixels were retained.

[19] The resulting classified images had a spatial resolution of 0.3 mm. An index of infiltration ice content (P_i, % mm^{-2}) was derived by averaging images across their row dimension and resampling at a 1-mm interval (Figures 5d and 6d). A fully wetted and refrozen layer has a P_i of 100% while a partially wetted/refrozen layer and discontinuous features such as ice glands have lower P_i values. Figure 5 shows an example where the automatic classification results matched closely those from the visual interpretation. In
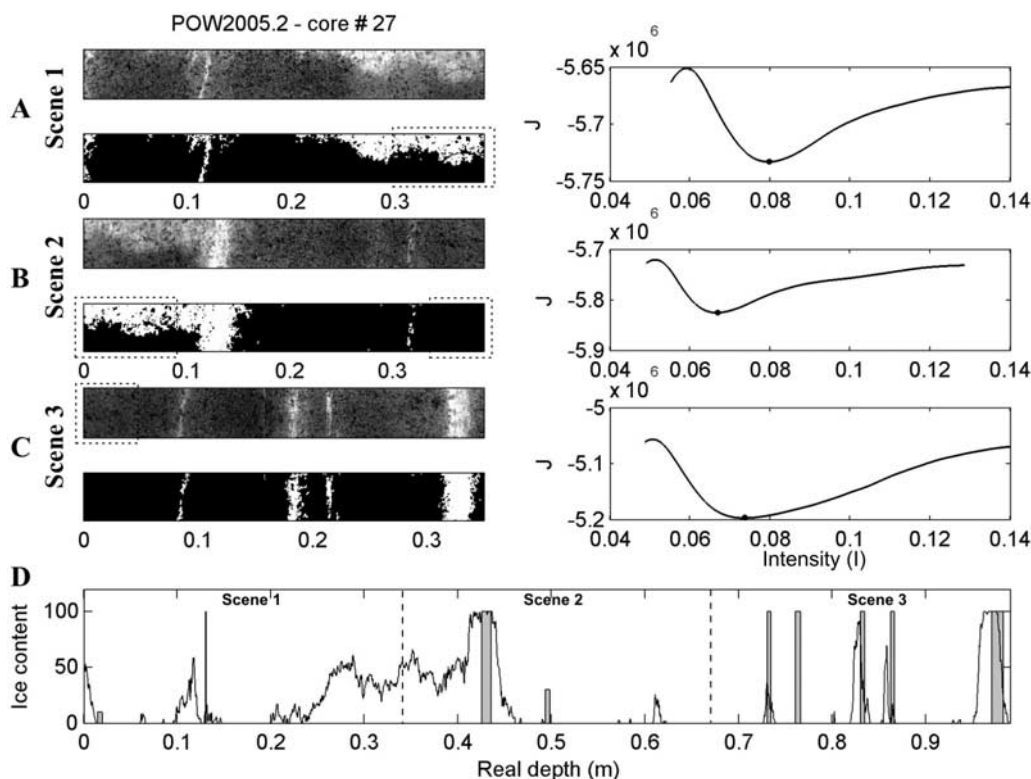
Figure 6. Same as Figure 5, but for core 27 (27.8–28.8 m depth).

other cases, the thresholding procedure detected partially refrozen zones in the core (e.g., an irregular ice gland) more accurately (Figures 6a and 6b). Such features are sometimes difficult to interpret by eye, but were objectively detected by the thresholding procedure.

[20] In Figure 7, the infiltration ice content index obtained from both methods was compared for each core segment. Although the two methods generally agree, there are significant differences. The optical method is more successful at detecting discontinuous features such as partially refrozen layers and ice glands. As an example, while both methods gave similar results for core 45 (triangle, Figure 7), the detection of the partially refrozen feature in core 27 resulted in significantly different average P_i values (star, Figure 7).

4.3. Effect of Melting on Glaciochemistry

[21] The high-resolution ice content index may be used to investigate the effect of melting on glaciochemical signals in the POW ice core. Here we used the high-resolution (5 mm) ECM record to look at the relationship between solid conductivity and ice facies. The ECM measures the acidity of the ice. In the Arctic this is mainly due to the deposition of sulphuric and nitric acids in snow, which are partly neutralized by alkaline dust [Hammer, 1980]. Melting causes leaching of ions in snowpacks, and strong acids are preferentially eluted compared to other major ions such as Na^+ [Davies et al., 1982; Koerner, 1997]. Thus melting can alter seasonal glaciochemical and ECM signals, and may compromise the identification of volcanic acidic horizons.

[22] Melt features observed in the core were all thinner than ∼50 cm, so the ECM record was high-pass filtered with a robust spline [Meeker et al., 1995] that removed all periodic variations longer than 1 m (Figures 8a and 8b). This, for example, compensated for increased snow acidity due to anthropogenic emissions of SO_x and NO_x in the recent industrial era [Koerner and Fisher, 1982]. Two methods were used to compare the filtered ECM signal with P_i. First, the P_i series was binned into 10% classes and the corresponding median ECM value was linearly regressed against the P_i classes. The data were binned because ECM values are unequally distributed over the P_i range and hence suffer from large heteroscedasticity. The median was used as an estimator of central tendency because the ECM distribution is skewed by spikes of volcanic origin. The median ECM signal was found to be linearly correlated ($r = 0.91$, $p < 0.05$) with the melting index (Figure 8c). Second, the ECM data were partitioned into two subsets, corresponding to infiltration and glacier ice, and a nonparametric Mann-Whitney test [e.g., Gibbons and Chakraborti, 2003] was used to assess whether the two subsets came from the same population (Figure 8d). The normal test statistic ($Z = 9.1$, $p < 0.01$) shows that the median ECM signal for infiltration ice is significantly larger than that for glacier ice. Repeating the process by partitioning the populations with successively higher P_i thresholds shows that the best separation between populations occurs at $P_i \geq 0.6$ ($Z = 14.1$, $p < 0.01$). An Ansari-Bradley test for homogeneity of variance [Gibbons and Chakraborti, 2003] indicates that the ECM signal in infiltration ice is more variable than in glacier ice, with again the greatest variance contrast for $P_i \geq 0.6$. Nonparametric tests were used since the data is nonnormally distributed. These results confirm that melting at the surface of the POW Icefield is causing elution of strong acids, which upon refreezing tend to
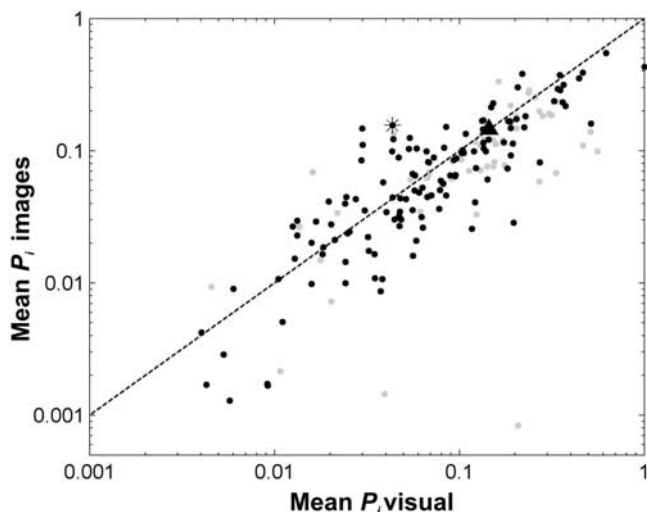
Figure 7. Core-wise average ice content from images versus that derived from visual interpretation. Stippled line is the 1:1 delineation. Black dots are for cores with no fractures, and gray dots are for fractured cores.

accumulate within melt features. This finding has important implications for the interpretation of ice core glaciochemical records [*Koerner*, 1997], which will be discussed next. The higher ECM variance in infiltration ice also shows that only

some, not all melt features have enhanced chemical concentrations. If the ECM probability distribution observed for glacier ice, $p(x)$, is assumed to be representative of ice unaffected by melt, then the probability $f(k|n, p)$ of observing more than k infiltration ice data points with an ECM value of x and probability of success $p(x)$ out of n total observations may be described by an inverse binomial cumulative distribution (Figure 8e). The density functions for both populations were estimated using a kernel smoothing method (Figure 8d). The probability f may be used to determine where the probability distributions from the two populations differ significantly. Melt features with ECM values >0.0145 have a 95% probability of being chemically enriched owing to elution (Figure 8e). Using the depth-time scale for the POW core, years when elution probably took place may then be identified (Figure 9a). The average annual melt percentage for the last 580 years is 9%. Surface melting at the coring site occurred in 8 years out of 10 and elution probably occurred in ~36% of these years. Hence, elution due to melt occurred on average 3 years out of 10.

[23] Using the density-corrected P_i index (defined in section 4.4) averaged over 1-year intervals, the distribution of annual melt fraction $P_i(t)$ for years with and without elution may be compared (Figure 9b). Although more elution events are associated with lower annual melt fractions, the probability of elution increases with the amount of melt, reaching 100% when $P_i(t) > 0.6$ (Figure 9c). These
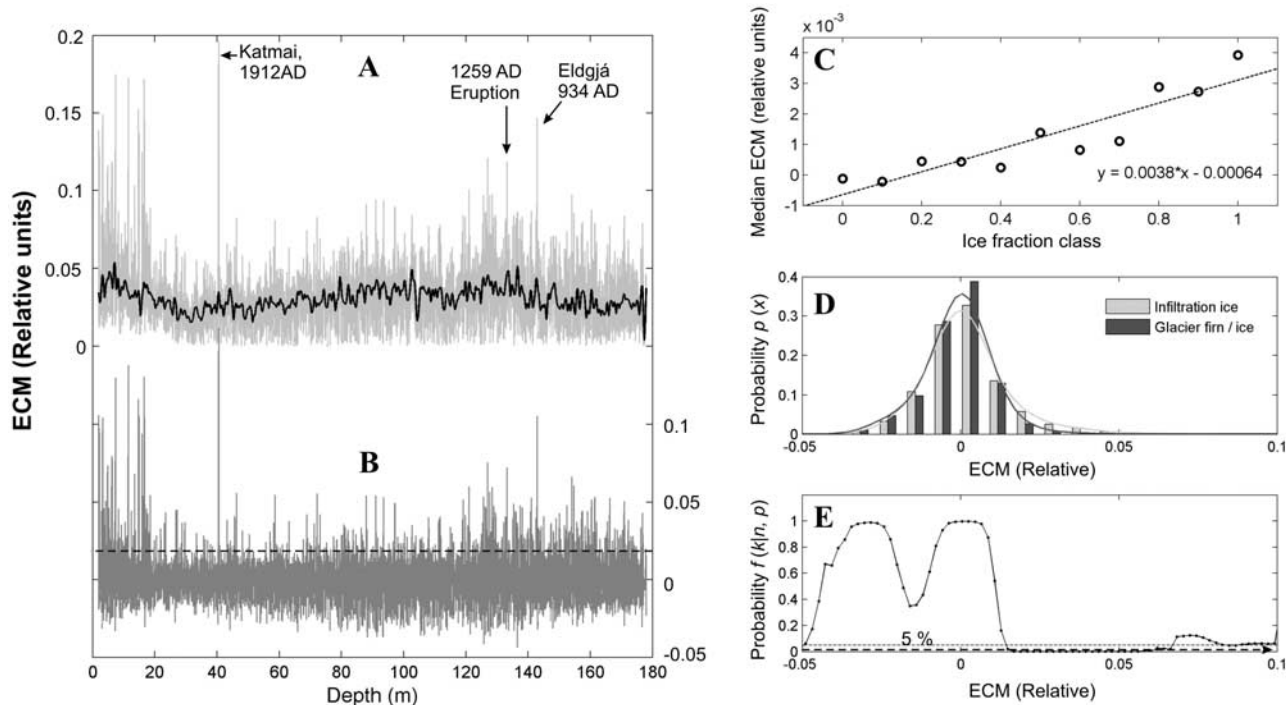

Figure 8. (a) The 5-mm-interval ECM record (gray line) with robust spline function (black line). (b) High-frequency residual ECM values, with calculated elution threshold (stippled line). (c) Median residual ECM versus ice fraction class. A class of 0−0.1 includes all samples with melt above 0 and below 0.1. (d) Histogram (bars) and density functions (stippled lines) of ECM values for glacier and infiltration ice. (e) Probability of observing more infiltration ice than glacier ice samples with a given ECM value. ECM values below the 5% threshold (stippled line) have a 95% probability of being chemically enriched owing to elution. The rise above the threshold for ECM values larger than 0.07 may be due to the strongly acidic volcanic layers and/or because of poor density estimation near the distribution tail.
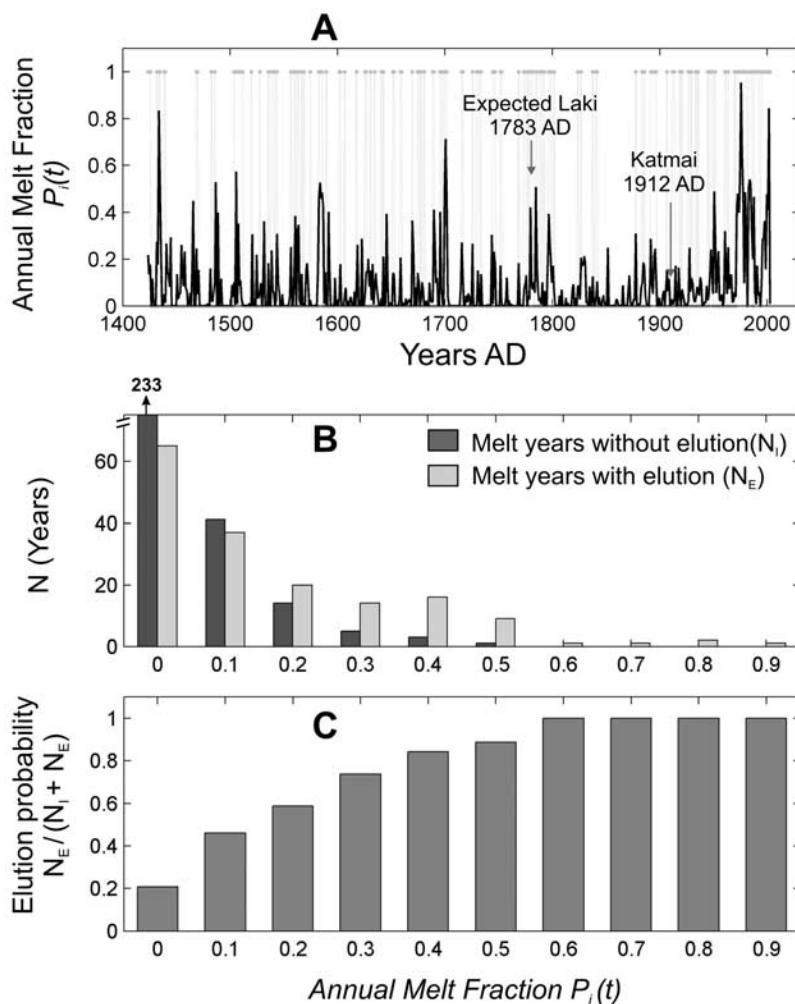
Figure 9. (a) Annual melt fraction for 1424–2004 A.D., corresponding to the upper 120 m of the core. Gray vertical dotted lines indicate years with probable elution. Also shown are the Katmai (observed) and Laki (expected) volcanic events. (b) Number of years per annual melt fraction class for years with (light gray) and without (dark gray) elution. A class of 0–0.1 includes all samples with melt above 0 and below 0.1. (c) Probability of elution occurrence per annual melt class.

results give an indication of the quality of signal preservation to be expected from the amount of melting taking place at the site, and are consistent with previous studies. *Grumet et al.* [1998] identified pseudoseasonal cycles in an ice core from Penny Ice Cap, Baffin Island, where the average melt percentage over the past 300 years is 40%. However, during periods when melt rose above 50–60% these signals were obliterated. In an ice core from the Lomonosovfonna ice field, Svalbard, with average melt of 55%, *Pohjola et al.* [2002] found that strong acids were eluted and accumulated in melt features, which obliterated any obvious seasonal cycles in the glaciochemical series.

[24] Seasonal melting on the POW Icefield also altered the volcanic signals present in the ECM record. While the acid peaks from the Katmai eruption and the 1259 A.D. event were clearly identified in a section of the core with low melt percentage (<4% a^{-1}) no peak could be found for other volcanic horizons commonly found in Arctic ice caps, such as Laki (1783 A.D.), which according to the timescale

occurred during a period with higher melt rates ($\sim$15% a^{-1}) (Figure 9a).

4.4. Melt History

[25] The melt index from the POW core may be used as a proxy for past summer warmth at the site [*Koerner*, 1977]. The ice content index P_i was first corrected for differential compaction with depth before averaging over time. The measured bulk density profile, smoothed with a robust spline, was used to convert firn to ice equivalent depths. The high-resolution proxy density profile was not used as it is only continuous above 75 m. The bias in P_i resulting from artificial compression of melt features when converting to ice depths was removed by multiplying P_i by the reciprocal of the smoothed density curve, $0.917/\rho$ [e.g., *Koerner and Fisher*, 1990]. The corrected P_i values were then averaged into 1- and 5-year intervals.

[26] Over the last 1000 years the annual melt percentage shows large decadal variability and a general cooling trend until $\sim$1850 A.D., after which melting increased progres-
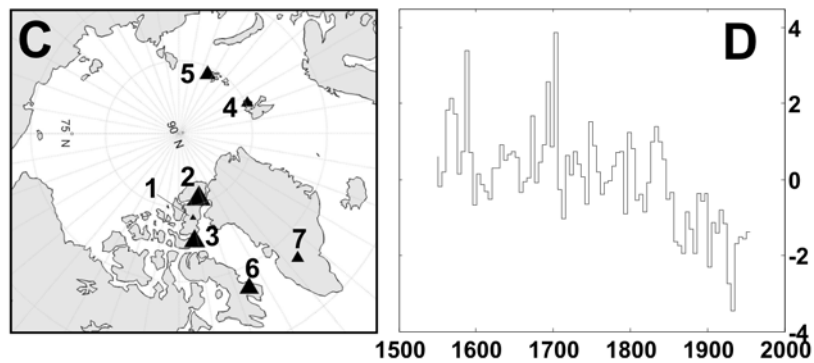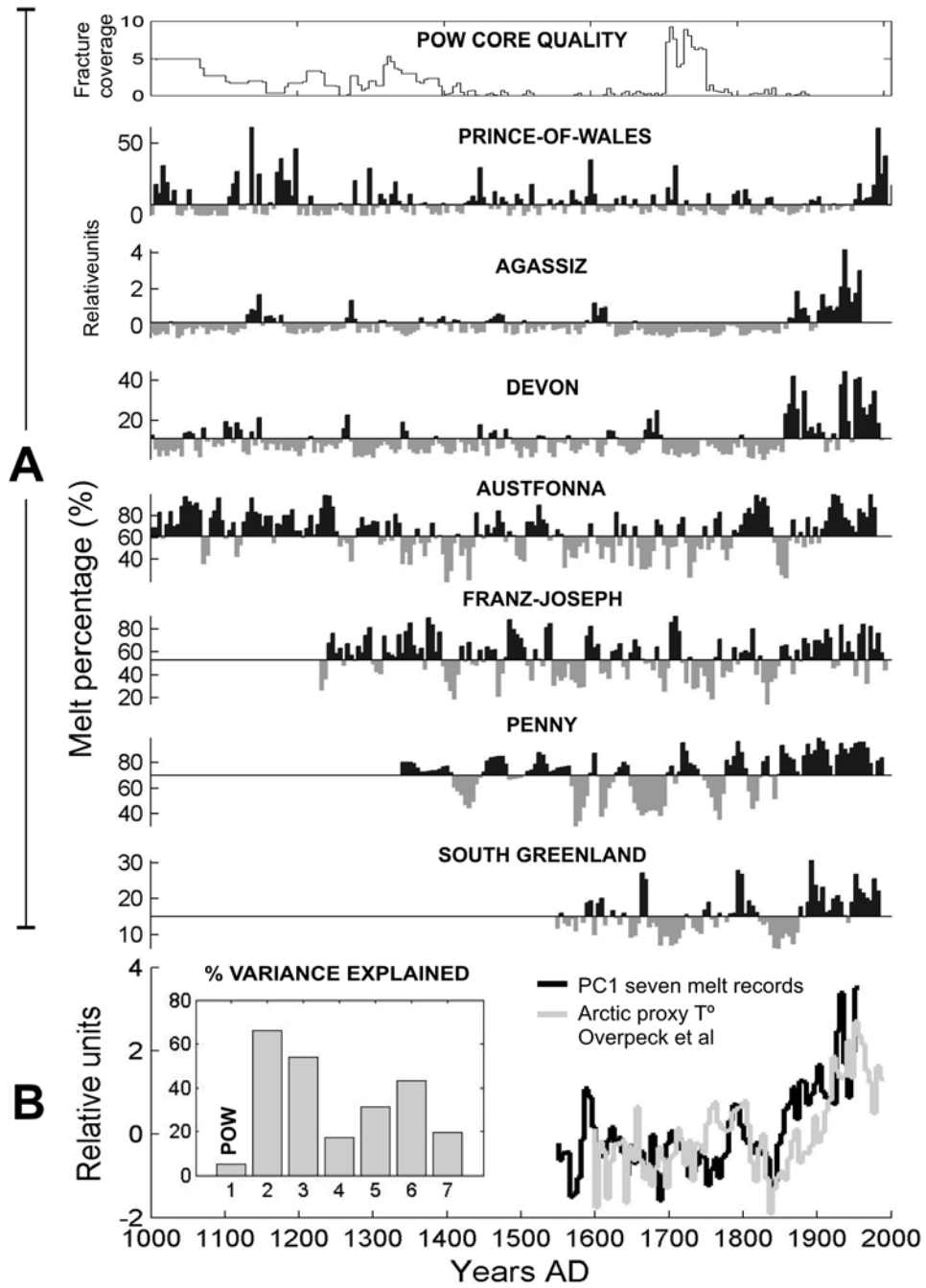
Figure 10

sively (Figure 10a). The 12th century and the second half of the 20th century are the periods with the highest and most sustained melt. Sections with poor core quality may underestimate the melting percentage, for example during the 1000–1100 A.D. and 1700–1750 A.D. intervals. Melt records from other Arctic ice caps were gathered and compared with the POW record (Figure 10a). The POW record is noticeably different from those from the nearby Agassiz (altitude 1730 m) and Devon ice caps (altitude 1800 m). Devon and Agassiz are ~750 km apart and the correlation between these melt records over the last 1000 years is 0.53, which is similar to that observed between air temperature records from Arctic weather stations separated by this distance [*Rigor et al.*, 2000]. However, the correlation between the POW record and these two sites, each ~375 km away, is close to zero. Furthermore, the lag-1 autocorrelation coefficients for the Agassiz and Devon records are 0.61 and 0.60, which is typical of temperature series [*Fisher*, 2002], but it is only 0.28 for the POW record, using either the visual or optical melt indices. The autocorrelation coefficient did not change significantly when calculated for periods with good core quality, so the varying core quality may explain part, but not all of the higher-frequency character of the POW record. Hence melt events on the POW Icefield appear to be mostly asynchronous with those at neighboring sites, and the record is also less "persistent" (smaller lag-1 autocorrelation) than is typically expected for temperature series, suggesting that melting episodes on the POW Icefield may be associated with local, rather than regional conditions.

[27] A principal components analysis was performed on the seven standardized Arctic melt records over their common time period 1551–1956 A.D. The first principal component (PC1) explains 34% of the total variance and is significantly different from red noise at the 95% significance level. PC1 is similar ($r = 0.60$, $p < 0.05$) to the Arctic summer proxy temperature reconstruction from *Overpeck et al.* [1997] and may be interpreted as the common response of the seven Arctic ice caps to pan-Arctic thermal forcing (Figure 10b). The loadings are positive for all sites and explain between 17% and 66% of the variance of individual series, except for the POW site where PC1 only accounts for 5% of the variance (Figure 10b). The amount of local variance explained reflects the contribution of local climate and glaciological processes. While most melt records show a post-1850 A.D. melt increase in response to a pan-Arctic temperature rise, the rate of increase in the POW record was comparatively slower. Only in recent decades has melt increased abruptly at this site.

[28] *Marshall et al.* [2007] have shown that on the summit of POW Icefield low-melt years occur together with steep surface temperature lapse rates, resembling moist adiabatic rates in free air, and enhanced cyclonic activity with a southerly flow aloft. In contrast, large melt was observed together with weak lapse rates and a northerly, anticyclonic flow aloft. Intermittent decoupling of surface climate conditions between the high and low elevations of the ice cap was also reported by *Wang et al.* [2005, Figure 3], who showed that interannual variability in the melt season length at high elevations on the POW Icefield was inverse to that at low elevations for the period 2000–2004. *Alt* [1987] and *Gardner and Sharp* [2007] showed that the shape, position and strength of the July polar vortex are determinant for mass balance conditions on Queen Elizabeth Islands (QEI) glaciers. Three main influential synoptic regimes are recognized: (1) contraction of the polar vortex and intrusion of a ridge into the QEI, bringing warm and dry air and causing extreme melting; (2) general expansion of the polar vortex, or its elongation across Ellesmere Island and down Baffin Bay, resulting in increased advection of cold/moist air from the Arctic Ocean, which suppresses melt and increases precipitation; and (3) Baffin Bay low-pressure center, which advects mild/moist air to the eastern QEI, overcast conditions, increased precipitation and generally negative mass balance conditions. In this last situation, melting may be enhanced at low elevations of ice caps owing to rainfall, but higher elevations receive more snow and melt may be limited by overcast conditions. Increased snow accumulation in summer will also raise the albedo of the ice cap surface and reduce melting. At present, the POW Icefield appears to be affected by the mild/moist climate of Baffin Bay on its eastern flank, and the varying influence of warm/dry continental and/or cold/moist Arctic Ocean air masses on its western side. The coring site is located near the boundary where melt anomalies at high and low elevations are of opposite signs [*Wang et al.*, 2005] and on the boundary between the drier, colder "Northern" region and the more maritime "Eastern" climatic region, as defined by *Maxwell* [1981]. The similarity of the Agassiz and Devon melt records, as well as their coherent response to pan-Arctic thermal forcing in summer, may imply that these two sites have remained in different but stable climatic zones over the past 1000 years. In contrast, the POW melt record may partly reflect the migration of the Baffin Bay climate boundary over time. The progressive shift from a more continental to a cooler, more maritime regime could explain the offset between the regional warming trend and the POW melt record.

[29] Another factor that is likely to impact locally on the climate of the POW Icefield is the proximity of the NOW polynya in northern Baffin Bay (see Figure 1). With an area of 80,000 km², it is the largest polynya in the Canadian Arctic [*Smith and Rigby*, 1981]. The polynya forms in winter when prevailing northerly winds push sea ice down

Figure 10. (a) Circum-Arctic melt record (5-year averages). The top panel displays the core quality index for POW. Data sources: Prince-of-Wales, this study; Agassiz, *Fisher and Koerner* [1994]; Devon, *Kinnard et al.* [2006]; Austfonna, *Tarussov* [1992]; Franz-Joseph, *Henderson* [2002]; Penny, *Okuyama et al.* [2003]; South Greenland, *Kameda et al.* [1995]. (b) First principal component (PC1) of the seven Arctic melt records (black line) and Arctic summer temperature reconstruction (gray line [*Overpeck et al.*, 1997]). The bar graph shows the percent variance explained in each melt record, with bar numbers referring to site numbers in Figure 10a. (c) Map of ice core sites; triangle size represent the percent variance explained by PC1. (d) Difference time series between the standardized POW melt and PC1 records.

Nares Strait, forming an ice bridge which blocks further ice advection to the South. The NOW polynya is not continually present, but nevertheless represents an important yet variable local source of heat and moisture for nearby glaciers and ice caps. This is reflected in the larger accumulation rate at the POW coring site (0.30 m ice a^{-1}) compared to Agassiz (0.175 m ice a^{-1}) and Devon (0.23 m ice a^{-1}) ice caps. Heat advection from the polynya would take place in winter when temperatures on the POW Icefield are well below freezing. However, it is likely that the timing of opening/closing and the areal extent of the polynya in spring and fall exert a control on the timing and amount of snow accumulating on the POW Icefield summit. *Barber et al.* [2001] showed that warm (cold) years tend to be associated with positive (negative) sea-ice concentration anomalies in the NOW polynya. This occurs because cold northerly winds favor ice export from, and opening of, the polynya, while warmer southerly wind restrict the advection of ice south of the polynya, limiting its extent.

[30] We estimated the contribution of site-specific process(es) to the melt history on the POW Icefield by subtracting the PC1 signal from the standardized POW melt record (Figure 10d). The resulting series exhibits pulse-like fluctuations, and a gradual decrease in melt after the early 1850s relative to PC1. This could be due to a local cooling feedback from Baffin Bay during summer, but observations suggest a warming in that area over 1916–2003 [*Zweng and Münchow*, 2006]. In light of the previous discussion, we suggest that the slow melt increase on the POW Icefield after ∼1850 when compared with the pan-Arctic trend, may reflect a growing influence of the Baffin Bay climate, and/or more open water conditions in the NOW polynya, causing increasing snow accumulation on the POW Icefield. An increase in accumulation rate while keeping the amount of seasonal melt constant would result in an apparent decreased melt percentage in the ice core (melt % = melt [cm a^{-1}]/ accumulation [cm a^{-1}]). Accumulation typically increases with warmer temperature and decreases with cooler temperature, so that changes in accumulation rate usually attenuate the melt-temperature relationship [*Koerner and Fisher*, 1990]. Unfortunately, long accumulation time series are not presently available for the POW Icefield to test this hypothesis, and neither are high-resolution proxy records of sea ice conditions in the NOW polynya to compare with the POW melt record. *Levac et al.* [2001] developed a coarse (centennial scale) reconstruction of sea-surface conditions in the NOW polynya from a sediment core from Smith Sound. Their analysis suggests an increase in open water conditions from 2 to 4 months per year over the last ∼200 years. We speculate that the post-1850 A.D. regional warming trend has caused a northward contraction of the midtropospheric summer polar vortex over the western Arctic while an elongated trough has remained over the eastern QEI [*Alt*, 1987; *Gardner and Sharp*, 2007]. This synoptic pattern favors the northward movement of cyclones into Baffin Bay which cause colder summers and milder winters [*Barry et al.*, 1975], and the concomitant opening of the NOW polynya [*Barber et al.*, 2001]. Hence colder (warmer) conditions would lead to larger (lower) precipitation on the POW Icefield due opening (closing) of the polynya. This coupling between atmospheric synoptic conditions and the wind-driven dynamic of the NOW polynya may then accentuate, and not attenuate [*Koerner and Fisher*, 1990], the melt-temperature relationship on the POW Icefield.

5. Conclusions

[31] The optical system and image analysis techniques developed in this study have proven useful for characterizing ice core stratigraphy at a high spatial resolution. The imaging apparatus uses a low-cost CCD digital camera and is easily implemented. However, the images derived suffer from various radiometric and geometric biases which need to be carefully corrected, and this work has provided methods to do so. The derived profile of transmitted light intensity is related to core density in a nonlinear way, as found by others [*Sjögren et al.*, 2007], an observation explained by the fact that light transmission depends on the total area of scattering ice-air interfaces, which vary with the densification process. The modeled relationship was used to produce a high-resolution (5 mm) proxy density profile for the core. Seasonal density variations, which are commonly found in the dry snow zones of ice caps, were only observed in a few sections of the core with low melt, so the original depositional sequence in the POW core has been mostly obliterated by melt.

[32] The melt features caused by infiltration and refreezing of meltwater appeared brighter in digital images, and were successfully discriminated with an automatic thresholding algorithm. Heavily fractured sections, however, confounded the algorithm and manual editing was necessary. The ice content index derived from the classified images was generally in good agreement with visual observations, but the image analysis method identified irregular melt features more accurately and is considered more objective.

[33] The optical ice content index was used to quantify the effect of melting on the solid conductivity of the ice core. A greater and more variable ECM signal was found in melt features compared to glacier ice, suggesting that elution of strong acids occurs at the site. A critical ECM threshold was derived to identify chemically enriched melt features and was used to identify periods in the record which probably suffered from elution. The annual probability that elution occurred was found to increase from 20% for annual melt percentages in the range >0–10%, to 100% when over 60% of the annual layer consists of infiltration ice. The alteration of glaciochemistry records by elution represents a significant problem in ice core studies. In this regard our results offer a useful estimate of the preservation of glaciochemical signals in ice cores recovered from the percolation zone of Arctic ice caps.

[34] The POW melt history, a proxy for past summer warmth, bears little resemblance to the melt histories from neighboring ice core sites or the common melt signal from seven circum-Arctic ice caps. This suggests that its signal is predominantly controlled by site-specific climatic or glaciological factors that we cannot resolve from the melt record alone. We propose that the varying influence of cyclonic conditions in Baffin Bay and associated steep lapse rates, as well as the intermittent opening and closing of the adjacent NOW polynya are the major control on the POW Icefield melt history.

References

Alley, R. B., et al. (1997), Visual stratigraphic dating of the GISP2 ice core: Basis, reproducibility, and application, *J. Geophys. Res.*, *102*(C12), 26,367–26,381, doi:10.1029/96JC03837.

Alt, B. T. (1987), Developing synoptic analogs for extreme mass balance conditions on Queen Elizabeth Island ice caps, *J. Clim. Appl. Meteorol.*, *26*(12), 1605–1623, doi:10.1175/1520-0450(1987)026<1605:DSAFEM>2.0.CO;2.

Barber, D. G., J. M. Hanesiak, W. Chan, and J. Piwowar (2001), Sea-ice and meteorological conditions in Northern Baffin Bay and the North Water Polynya between 1979 and 1996, *Atmos. Ocean*, *39*(3), 343–359.

Barry, R. G., R. S. Bradley, and J. D. Jacobs (1975), Synoptic climatological studies of the Baffin island Area, in *Climate of the Arctic*, edited by G. Weller and S. A. Bowling, pp. 82–90, Geophys. Inst. Univ. of Alaska, Fairbanks.

Bohren, C. F., and B. R. Barkstrom (1974), Theory of the optical properties of snow, *J. Geophys. Res.*, *79*(30), 4527–4535, doi:10.1029/JC079i030p04527.

Cho, S., R. Haralick, and S. Yi (1989), Improvement of Kittler and Illingworths minimum error thresholding, *Pattern Recognit.*, *22*(5), 609–617, doi:10.1016/0031-3203(89)90029-0.

Cooper, M. C. (1998), The use of digital image analysis in the study of laminated sediments, *J. Paleolimnol.*, *19*, 33–40, doi:10.1023/A:1007912417389.

Dansgaard, W., and S. J. Johnsen (1969), A flow model and a timescale for the ice core from Camp Century, Greenland, *J. Glaciol.*, *8*, 215–223.

Davies, T. D., C. E. Vincent, and P. Brimblecombe (1982), Preferential elution of strong acids from a Norwegian ice cap, *Nature*, *300*, 161–163, doi:10.1038/300161a0.

Domine, F., M. Albert, T. Huthwelker, H.-W. Jacobi, A. A. Kokhanovsky, M. Lehning, G. Picard, and W. R. Simpson (2008), Snow physics as relevant to snow photochemistry, *Atmos. Chem. Phys.*, *8*, 171–208.

Fisher, D. A. (2002), High-resolution multiproxy climatic records from ice cores, tree-rings, corals and documentary sources using eigenvector techniques and maps: Assessment of recovered signal and errors, *Holocene*, *12*(4), 401–419, doi:10.1191/0959683602hl546rp.

Fisher, D. A., and R. M. Koerner (1994), Signal and noise in four ice-core records from the Agassiz ice cap, Ellesmere Island, Canada: Details of the last millennium for stable isotopes, melt and solid conductivity, *Holocene*, *4*(2), 113–120, doi:10.1177/095968369400400201.

Gardner, A. S., and M. J. Sharp (2007), Influence of the Arctic circumpolar vortex on the mass balance of Canadian high Arctic glaciers, *J. Clim.*, *20*, 4586–4598, doi:10.1175/JCLI4268.1.

Gibbons, J. D., and S. Chakraborti (2003), *Nonparametric Statistical Inference*, 4th ed., Marcel Dekker, New York.

Gow, A. J. (1969), On the rates of growth of grains and crystals in South Polar firn, *J. Glaciol.*, *8*, 241–252.

Gow, A. J. (1975), Time-temperature dependence of sintering in perennial isothermal snowpacks, in *Proceedings of the Grindewald Symposium, April 1974, IAHS Publ. No. 114*, pp. 25–41, Int. Assoc. of Hydrol. Sci., Gentbrugge, Belgium.

Grumet, N. S., C. P. Wake, G. A. Zielinski, D. Fisher, R. Koerner, and J. D. Jacobs (1998), Preservation of glaciochemical time-series in snow and ice from the Penny Ice Cap, Baffin Island, *Geophys. Res. Lett.*, *25*(3), 357–360, doi:10.1029/97GL03787.

Hammer, C. U. (1980), Acidity of polar ice cores in relation to absolute dating, past volcanism, and radio-echoes, *J. Glaciol.*, *25*, 359–372.

Hawley, R. L., and E. Morris (2006), Borehole optical stratigraphy and neutron-scattering density measurements at Summit, Greenland, *J. Glaciol.*, *52*, 491–496, doi:10.3189/172756506781828368.

Hawley, R. L., E. D. Waddington, R. B. Alley, and K. C. Taylor (2003), Annual layers in polar firn detected by borehole optical stratigraphy, *Geophys. Res. Lett.*, *30*(15), 1788, doi:10.1029/2003GL017675.

Henderson, K. A. (2002), An ice core paleoclimate study of Windy Dome, Franz Josef Land (Russia): Development of a recent climate history for the Barent Sea, Ph.D. diss., 218 pp., Ohio State Univ., Columbus.

Herron, M. M., S. L. Herron, and C. C. Langway (1981), Climatic signal of ice melt features in southern Greenland, *Nature*, *293*, 389–391, doi:10.1038/293389a0.

Hori, A., et al. (1999), A detailed density profile of the Dome Fuji (Antarctica) shallow ice core by X-ray transmission method, *Ann. Glaciol.*, *29*, 211–214, doi:10.3189/172756499781821157.

Kaczmarska, M., E. Isaksson, L. Karlöf, O. Brandt, J.-G. Winther, R. S. W. Van De Wal, M. Van Den Broeke, and S. J. Johnsen (2006), Ice core melt features in relation to Antarctic coastal climate, *Antarct. Sci.*, *18*(2), 271–278, doi:10.1017/S0954102006000319.

Kameda, T., H. Narita, H. Shoji, F. Nishio, Y. Fujii, and O. Watanabe (1995), Melt features in ice cores from Site J, southern Greenland: Some implications for summer climate since AD 1550, *Ann. Glaciol.*, *21*, 51–58.

Kawamura, T. (1990), Nondestructive, three-dimensional density measurements of ice core samples by x ray computed tomography, *J. Geophys. Res.*, *95*(B8), 12,407–12,412, doi:10.1029/JB095iB08p12407.

Kinnard, C., C. M. Zdanowicz, D. A. Fisher, and C. P. Wake (2006), Calibration of an ice-core glaciochemical (sea-salt) record with sea-ice variability in the Canadian Arctic, *Ann. Glaciol.*, *44*, 383–390, doi:10.3189/172756406781811349.

Kittler, J., and J. Illingworth (1986), Minimum error thresholding, *Pattern Recognit.*, *19*(1), 41–47, doi:10.1016/0031-3203(86)90030-0.

Koerner, R. M. (1977), Devon Island ice cap: Core stratigraphy and paleoclimate, *Science*, *196*(4285), 15–18, doi:10.1126/science.196.4285.15.

Koerner, R. M. (1997), Some comments on climatic reconstructions from ice cores drilled in areas of high melt, *J. Glaciol.*, *43*, 90–97.

Koerner, R. M., and D. A. Fisher (1982), Acid snow in the Canadian high Arctic, *Nature*, *295*, 137–140, doi:10.1038/295137a0.

Koerner, R. M., and D. A. Fisher (1990), A record of Holocene summer climate from a Canadian high-Arctic ice core, *Nature*, *343*, 630–631, doi:10.1038/343630a0.

Kokhanovsky, A. A., and E. P. Zege (2004), Scattering optics of snow, *Appl. Opt.*, *43*(7), 1589–1602, doi:10.1364/AO.43.001589.

Langway, C. C. (1970), Stratigraphic analysis of a deep ice core from Greenland, *Spec. Pap. Geol. Soc. Am.*, *125*, 186 pp.

Levac, E., A. De Vernal, and W. Blake (2001), Sea-surface conditions in northernmost Baffin Bay during the Holocene: Palynological evidence, *J. Quat. Sci.*, *16*(4), 353–363, doi:10.1002/jqs.614.

Marshall, S. J., M. J. Sharp, D. O. Burgess, and F. S. Anslow (2007), Near-surface-temperature lapse rates on the Prince of Wales Icefield, Ellesmere Island, Canada: Implications for regional downscaling of temperature, *Int. J. Climatol.*, *27*(3), 385–398, doi:10.1002/joc.1396.

Maxwell, J. B. (1981), Climatic regions of the Canadian Arctic Islands, *Arctic*, *34*(3), 225–240.

Meeker, L. D., P. A. Mayewski, and P. Bloomfield (1995), A new approach to glaciochemical time series analysis, in *Ice Core Studies of Global Biogeochemical Cycles*, edited by R. J. Delmas, pp. 383–400, Springer, Berlin.

Meese, D. A., A. J. Gow, R. B. Alley, G. A. Zielinski, P. M. Grootes, M. Ram, K. C. Taylor, P. A. Mayewski, and J. F. Bolzan (1997), The Greenland Ice Sheet Project 2 depth-age scale: Methods and results, *J. Geophys. Res.*, *102*(C12), 26,411–26,423, doi:10.1029/97JC00269.

Mellor, M. (1977), Engineering properties of snow, *J. Glaciol.*, *19*, 15–66.

Nederbragt, A. J., and J. W. Thurow (2004), Digital sediment colour analysis as a method to obtain high resolution climate proxy records, in *Image Analysis, Sediments and Paleoenvironments*, edited by P. Francus, pp. 105–124, Kluwer Acad., Dordrecht, Netherlands.

Okuyama, J., H. Narita, T. Hondoh, and R. M. Koerner (2003), Physical properties of the P96 ice core from Penny ice cap, Baffin Island, Canada, and derived climatic records, *J. Geophys. Res.*, *108*(B2), 2090, doi:10.1029/2001JB001707.

Overpeck, J., et al. (1997), Arctic environmental change of the last four centuries, *Science*, *278*(5341), 1251–1255, doi:10.1126/science.278.5341.1251.

Paterson, W. S. B. (1994), *The Physics of Glaciers*, 3rd ed., 480 pp., Pergamon, U.K.

Pohjola, V. A., J. C. Moore, E. Isaksson, T. Jauhiainen, R. S. W. van de Wal, T. Martma, H. A. J. Meijer, and R. Vaikmäe (2002), Effect of periodic melting on geochemical and isotopic signals in an ice core from Lomonosovfonna, Svalbard, *J. Geophys. Res.*, *107*(D4), 4036, doi:10.1029/2000JD000149.

Rigor, I. G., R. L. Colony, and S. Martin (2000), Variations in surface air temperature observations in the Arctic, 1979–97, *J. Clim.*, *13*, 896–914, doi:10.1175/1520-0442(2000)013<0896:VISATO>2.0.CO;2.

Russ, J. C. (2002), *The Image Processing Handbook*, 4th ed., 732 pp., CRC Press, London.

Sezgin, M., and B. Sankur (2004), Survey over image thresholding techniques and quantitative performance evaluation, *J. Electron. Imaging*, *13*(1), 146–168, doi:10.1117/1.1631315.

Sjögren, B., O. Brandt, C. Nuth, E. Isaksson, V. Pohjola, J. Kohler, and R. S. W. Van De Wal (2007), Determination of firn density in ice cores using image analysis, *J. Glaciol.*, *53*, 413–419, doi:10.3189/002214307783258369.

Smith, M., and B. Rigby (1981), Distribution of polynyas in the Canadian Arctic, in *Polynyas in the Canadian Arctic*, edited by I. Stirling and H. Cleator, *Occas. Pap. 45*, pp. 7–28, Can. Wildlife Serv., Ottawa.

Svensson, A., S. W. Nielsen, S. Kipfstuhl, S. J. Johnsen, J. P. Steffensen, M. Bigler, U. Ruth, and R. Röthlisberger (2005), Visual stratigraphy of the North Greenland Ice Core Project (NorthGRIP) ice core during the last glacial period, *J. Geophys. Res.*, *110*, D02108, doi:10.1029/2004JD005134.

Takata, M., Y. Iizuka, T. Hondoh, S. Fujita, Y. Fujii, and H. Shoji (2004), Stratigraphic analysis of Dome Fuji Antarctic ice core using an optical scanner, *Ann. Glaciol.*, *39*, 467–472, doi:10.3189/172756404781813899.

Tarussov, A. (1992), The Arctic from Svalbard to Severnaya Zemlya: Climatic reconstructions from ice cores, in *Climate Since AD 1500*, edited by R. S. Bradley and P. D. Jones, pp. 505–516, Routledge, London.

Vinther, B. M., et al. (2006), A synchronized dating of three Greenland ice cores throughout the Holocene, *J. Geophys. Res.*, *111*, D13102, doi:10.1029/2005JD006921.

Wang, L., M. J. Sharp, B. Rivard, S. Marshall, and D. Burgess (2005), Melt season duration on Canadian Arctic ice caps, 2000–2004, *Geophys. Res. Lett.*, *32*, L19502, doi:10.1029/2005GL023962.

Warren, S. G. (1982), Optical properties of snow, *Rev. Geophys.*, *20*, 67–89, doi:10.1029/RG020i001p00067.

Zheng, J., A. Kudo, D. A. Fisher, E. W. Blake, and M. Gerasimoff (1998), Solid electrical conductivity (ECM) from four Agassiz ice cores, Ellesmere Island, NWT, Canada: High-resolution signal and noise over the last millennium and low resolution over the Holocene, *Holocene*, *8*(4), 413–421, doi:10.1191/095968398676187747.

Zielinski, G. A., P. A. Mayewski, L. D. Meeker, S. Whitlow, M. S. Twickler, M. Morrison, D. A. Meese, A. J. Gow, and R. B. Alley (1994), Record of volcanism since 7000 B.C. from the GISP2 Greenland Ice Core and implications for the volcano-climate system, *Science*, *264*(5161), 948–952, doi:10.1126/science.264.5161.948.

Zweng, M. M., and A. Münchow (2006), Warming and freshening of Baffin Bay, 1916–2003, *J. Geophys. Res.*, *111*, C07016, doi:10.1029/2005JC003093.

———————————

D. A. Fisher, C. M. Zdanowicz, and J. Zheng, Geological Survey of Canada, Natural Resources Canada, 562 Booth Street, Ottawa, ON K1A 0E4, Canada. (fisher@nrcan-rncan.gc.ca; czdanowi@nrcan.gc.ca; jzheng@nrcan-rncan.gc.ca)

C. Kinnard and B. Lauriol, Department of Geography, University of Ottawa, Simard Hall, Room 047, 60 University, Ottawa, ON K1N 6N5, Canada. (ckinn045@uottawa.ca; blauriol@uottawa.ca)

L. Nicholson and M. J. Sharp, Department of Earth and Atmospheric Sciences, University of Alberta, 1-26 Earth Sciences Building, Edmonton, AB T6G 2E3, Canada. (linznix@gmail.com; Martin.sharp@ualberta.ca)